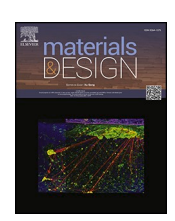
ELSEVIER

Contents lists available at ScienceDirect

# Materials & Design

journal homepage: www.elsevier.com/locate/matdes



# Development and characterisation of a liquid phase assisted healable aluminium-magnesium alloy processed by Laser Powder Bed Fusion

Julie Gheysen <sup>a,\*</sup>, Grzegorz Pyka <sup>a</sup>, Bartłomiej Winiarski <sup>b</sup>, Julie Villanova <sup>c</sup>, Florent Hannard <sup>a</sup>, Sophie De Raedemacker <sup>a</sup>, Jack Donoghue <sup>d</sup>, Albert Smith <sup>e</sup>, Aude Simar <sup>a</sup>

- a Institute of Mechanics, Materials and Civil Engineering, UCLouvain, Louvain-la-Neuve, Belgium
- <sup>b</sup> ThermoFisher Scientific, 627 00 Brno, Czech Republic
- <sup>c</sup> ESRF The European Synchrotron, CS 40220, 38043, Grenoble Cedex 9, France
- <sup>d</sup> University of Manchester, Manchester, United Kingdom
- e TESCAN-UK, Cambridge, United Kingdom

### ARTICLE INFO

### Keywords: Self-healing Aluminium alloys Additive manufacturing Liquid assisted healable alloys Correlative tomography

### ABSTRACT

Strategies to prevent the failure of Al alloys usually aim to optimise composition and microstructure to minimise damage initiation and propagation. However, these are inherently limited in that any damage that nucleates will not disappear. A new liquid phase assisted healable Al-Mg alloy is designed. Its microstructure is composed of a network of a lower melting point eutectic phase distributed within a higher melting point matrix. After damage, a healing heat treatment is applied at a temperature higher than the solidus temperature leading to liquid flow towards the damage sites and their welding. The matrix remains solid maintaining the structural integrity of the component. Correlative tomography combining insights from different 3D electron and X-ray nano-imaging techniques on the same volume of interest before and after healing, highlighted the complete healing and welding of voids and cracks up to 2  $\mu$ m within the Al-Mg alloy. While softening mechanisms are typically associated with heat treatments of Al alloys, this Al-Mg alloy also maintains strength and ductility after healing heat treatment. This promising concept to increase parts lifetime has potential to be extendable to other noneutectic 3D printed alloys.

### 1. Introduction

The traditional strategy to increase the lifetime of metallic parts has mainly been using thermo-mechanical treatments and alloying to develop microstructures that minimise damage initiation and propagation. However, defects which lead to premature failure of the part, may already be present in parts before their use, for instance those induced during manufacturing, such as porosities or cracks due to hot cracking during Laser Powder Bed Fusion (LPBF) [1]. Damage prevention strategies are therefore inherently limited as any damage that nucleates will not disappear [2]. It remains thus a major challenge to increase the lifetime of metallic products, such as for high strength Al alloys with low damage tolerance.

One strategy that is commonly used, specifically to close these manufacturing defects such as porosities in LPBF, is Hot Isostatic Pressing (HIP), i.e. a heat treatment under hydrostatic pressure in an inert atmosphere [3]. This compresses the part in order to close the voids and therefore, to increase the density of the part and delay fatigue crack nucleation. Although HIP has shown promising results as post-treatment on steel [4], nickel [5] and titanium [6–9] alloys, it is detrimental for Al alloys [10-12] due to the presence of an oxide film on the surfaces of the voids [13]. This is why, a liquid assisted HIP strategy was developed in our previous paper in order to tackle this issue [14]. It consists of a regular HIP treatment but at a temperature selected in the mushy zone of the alloy in order to induce its partial melting. This combines therefore, void closure due to the pressure of the HIP treatment with complete welding of the defects by the liquid phase. However, HIP has also significant drawbacks. First, the application of high pressure in an inert atmosphere significantly contributes to the part cost and repairing time, especially for large parts. Then, the HIP treatment requires the part to be removed from the installation. Finally, it may also lead to distortions of the part. This can be feasible as a post-processing step to heal all the

E-mail address: julie.gheysen@epfl.ch (J. Gheysen).

https://doi.org/10.1016/j.matdes.2025.114573

<sup>\*</sup> Corresponding author.

manufacturing defects, but it is certainly adding many maintenance steps during the service life of a part.

Another promising approach is based on the use of "Self-healing materials" where defect formation is accepted as long as it is counteracted by a process to remove them [15]. This bioinspired concept consists in the generation of a mobile phase called healing agent (HA) which migrates towards the crack and fills it. It is already well established and commercialised for polymers [16] but designing healable metallic alloys is more challenging due to the low mobility of metallic atoms at room temperature. An external driving force, typically a heat treatment, is therefore usually required to trigger this HA mobility [17]. Two categories of healing strategies are considered for metallic alloys [17].

First, the microscopic strategies are based on diffusion of solute atoms that act as HA. Their main limitation is the restricted amount of solute HA which can only heal nanometric damage sites [18,19]. This HA should also selectively precipitate on the damaged sites and not in the stable secondary phases throughout the matrix. Indeed, this would consume the HA which would then not be available to participate to the healing process anymore. Moreover, inhomogeneous healing is expected as faster healing occurs for damage located on diffusion short-cuts such as for example grain boundaries or dislocations. All these drawbacks impede the use and development of microscopic healable alloys.

Second, the macroscopic strategies are based on the flow of a liquid HA. This increases the amount and mobility of the HA compared to the previously described diffusion-based healing strategies and should therefore allow the healing of larger damage. There are three different ways to incorporate this liquid HA in the material. Firstly, it can be encapsulated inside ceramic tubes or capsules which can be released when a crack propagates and breaks the container [20,21]. This means that if the tube or capsule is not broken during the damage of the part, no healing will occur. Moreover, a good bonding between the HA and the matrix is required to efficiently stop the crack propagation [21]. Secondly, the HA can be deposited as a coating on the part [22,23].

However, it is not well investigated as only non-oxidised surfaces can be healed which is rarely the case [17]. Finally, the HA can be a low melting point phase inside the material [24]. This was investigated in the literature in the case of Sn-Bi solder alloys for microelectronic devices [25–27] and complete healing of the crack could not be achieved.

In this work, criteria were proposed to select promising alloying elements for liquid assisted healable Al alloys. A structural liquid assisted healable aluminium alloy is then developed based on these criteria and its healability is fully characterised thanks to 3D in-situ high resolution correlative techniques. The effectiveness of the healing abilities of this new alloy were demonstrated, providing insights into the development of healable Al alloys.

### 2. Design approach

The liquid phase assisted healable Al alloy developed in this work, see Fig. 1a, mimics the HA delivery from vascular networks of living systems. The microstructure is indeed composed of an interconnected network of low melting point eutectic phases (in dark grey on Fig. 1a), melting during healing heat treatment (HHT) and ensuring efficient transport of HA towards damage sites (Fig. 1c). This HA network is distributed within a "structural matrix" composed of a higher melting point phase which can be dendritic or cellular (depending on the solidification conditions, Fig. S3). This high melting point phase is remaining solid during healing and maintaining the structural integrity of the component. During service life, an overload can initiate damage on the strong but less ductile vascular network (Fig. 1b). It is important that this damage initiates directly at the boundaries of this network, as it makes it highly accessible to the HA allowing efficient and fast healing of damage. Indeed, if damage is located inside the high melting point phase, it will not be possible for the liquid HA to access it. In that unfavourable case only the slow diffusion healing mechanism could be activated. Afterwards, a HHT is applied above the eutectic temperature

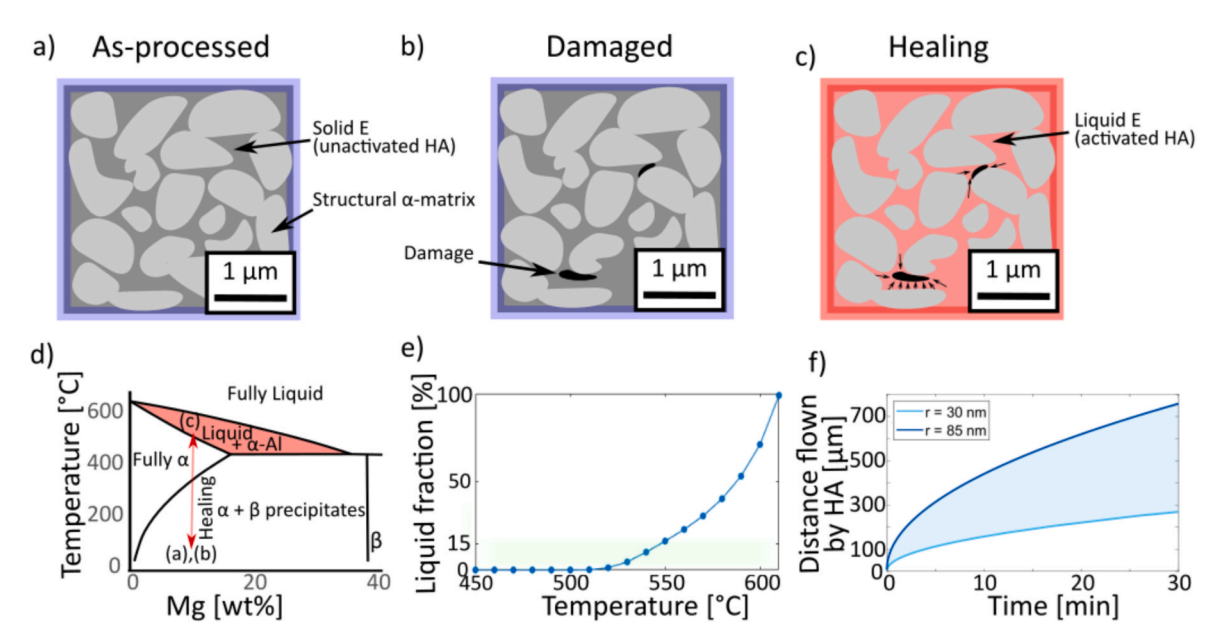
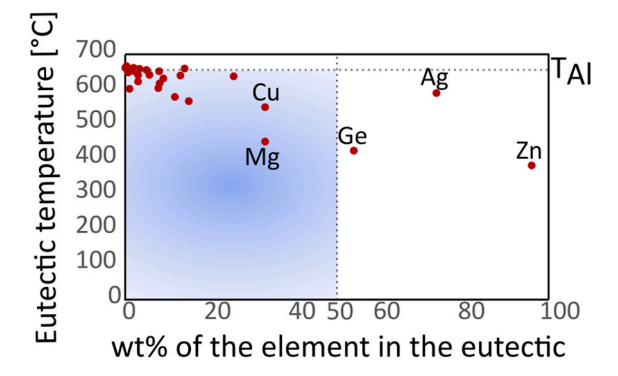


Fig. 1. Schematic representation of the microstructure in a) the as-processed state, b) damaged state and c) during liquid assisted healing. It is composed of a structural  $\alpha$ -Al matrix (in light grey) surrounded by the eutectic network E (in dark grey) which will play the role of healing agent (HA). The black represents the damage sites initiated at the boundaries of the eutectic network and the red the melted HA which can flow towards the damage. The blue and red boxes represent the room temperature and healing temperature conditions, respectively. d) Part of the binary phase diagram of the Al-Mg system with the healing conditions in red. e) Percentage of liquid fraction of HA in AlMg8 as a function of the temperature measured by Differential Scanning Calorimetry (DSC) and f) distance travelled by capillarity flow of pure liquid Al at 660 °C (surface tension of 850 mN/m, viscosity of 1.30 mPa • s and contact angle assumed to be 0° [28]) through a horizontal single capillarity tube of uniform circular cross-section not in contact with the atmosphere (gravity and atmospheric pressure neglected) calculated using the Washburn Equation [29] as a function of time for two network radii (r) 30 and 85 mm, corresponding to the eutectic network thickness (Fig. 3). The blue area in f) corresponds to the predicted distance that the HA should travel in the LPBF AlMg8 alloy studied in this work. (For interpretation of the references to colour in this figure legend, the reader is referred to the web version of this article.)

 $T_{\rm E}$  (Fig. 1c and d) to induce the melting of the HA. After this HA activation by local melting, the HA starts to flow by capillarity along the network, fills and accumulates inside the damage sites that was initiated at the boundaries the network itself, while the high melting point structural matrix remains in the solid state hence maintaining the structural integrity of the part. Upon cooling of the component, the solidification of the HA effectively welds the surfaces of the void back together and the part is healed.

One advantage of this strategy compared to the other microscopic (based on diffusion of HA) and macroscopic strategies (with HA in containers or deposited as a coating), is that it requires eutectic microstructures which can be manufactured using classical methods. Up to now, liquid phase assisted healable Sn-Bi alloys have only been produced using conventional casting [25,26]. However, these cast alloys present coarse microstructures with large and disconnected eutectic phases embedded in the structural matrix. In order to reduce the time required by the HA to flow towards the damage sites, and so increase the healing efficiency, a thinner and more interconnected eutectic network would be beneficial. This can be achieved using LPBF which leads to a very fine eutectic network with high connectivity resulting from its high cooling rate and thermal gradient (see Supplementary Material Fig. S1) [30]. The maximum distance that the liquid HA should flow to reach a damage site, i.e. to the middle of an  $\alpha$ -Al cell, increases actually from less than 1 µm in the thin microstructure of LPBF AlMg8, i.e. the alloy that will be investigated in this paper, to about 150 µm in cast AlMg8. Experiments and more information about the healing of cast AlMg8 compared to LPBF AlMg8 can be found in Supplementary Material Section 1. LPBF is thus a technology of choice to manufacture this new class of bioinspired healable alloys with vascular network of HA similar to the human body [31]. It was therefore used in the rest of this paper to manufacture the investigated eutectic-based healable alloy.

The binary Al-Mg system was selected as a good proof-of-concept alloy for our healing approach as its eutectic temperature (450 °C) is much lower than the one of  $\alpha$ -Al phase (660 °C) (Fig. 1d and Fig. 2). The Al-Mg system allows therefore to significantly reduce the melting temperature of the eutectic HA compared to other possible alloying elements in Al (Fig. 2). In order to obtain this two-phases microstructure, the composition must be hypo-eutectic (Mg < 33 wt% Fig. 1d). Indeed, a hyper-eutectic Al-Mg alloy would present similar melting temperatures for the HA and the structural matrix (Fig. 1d), leading thus to the complete melting of the material instead of its healing. A 8 wt% Mg composition was selected as a proof-of-concept, similarly to the one used in our previous work about liquid healing HIP [14] and which already showed a liquid healing potential in presence of hydrostatic pressure.



**Fig. 2.** Eutectic temperatures of alloying elements in Al as a function of their eutectic composition, data from Ref. [32]. The blue area contains the eutectic temperatures lower than the Al melting temperature (660  $^{\circ}$ C) and the compositions with a majority of Al compared to the alloying element at the eutectic composition, i.e. Al alloys. This blue area contains therefore the metallic alloys of interest for the development of a low melting point healable Al alloy. (For interpretation of the references to colour in this figure legend, the reader is referred to the web version of this article.)

Indeed, this composition significantly decreases the hot cracking susceptibility compared to lower Mg contents [30] and allows avoiding excessive amount of HA during HHT which leads to distortion due to insufficient structural matrix (see Supplementary Material Fig. S4).

### 3. Materials and methods

#### 3.1. Materials

The AlMg8 composition investigated in this paper was obtained by mixing pure aluminium provided by 3D Systems (purity >99.7%) with 14 wt% of pure Mg provided by SFM (purity >99.8%) in a Turbula powder blender for at least two hours. Mg was introduced in excess in order to compensate for the evaporation of Mg during the process. The homogeneity of the powder mixes was checked by Inductively coupled plasma optical emission spectroscopy 5100 (Agilent, USA) on three different mixture samples of each powder mix. The obtained chemical composition was Al (balance), Mg (13.7  $\pm$  0.1 wt%), Si (0.05  $\pm$  0.01 wt%)) and Fe (0.1  $\pm$  0.01 wt%), which leads to a final composition of the manufactured parts (i.e. after LPBF) of Al-8.4 wt%Mg designated as AlMg8 in this paper. The particle size distribution of the powder mix, measured by laser diffraction granulometry in a wet dispersion machine LS100Q (Beckman Coulter Inc, USA), is from 14.3  $\mu m$  to 57.8  $\mu m$  with a mean value of 35.5  $\mu m$ .

# 3.2. Manufacturing

The manufacturing of the samples was performed by Laser Powder Bed Fusion (LPBF) on a ProX200 machine (3D Systems, USA). It is composed of a laser with a wavelength of 1070 nm and a maximum power of 273 W. The build plate of the LPBF machine is not heated and the fabrication volume was  $140 \times 140 \times 125$  mm. All the samples were built under argon inert atmosphere, and the oxygen content was kept below 500 ppm.

The scanning strategy was composed of hexagons of 5 mm size, with an overlap of 100  $\mu$ m. The LPBF parameters were optimised using the methodology published by Gheysen *et al.* [33] leading to a laser power P of 216 W, a scanning speed v of 500 mm/s, a hatching space HS of 75  $\mu$ m and a layer thickness t of 30  $\mu$ m (see Supplementary Material Section 4).

### 3.3. Characterisation

The microstructural analysis was performed by scanning electron microscopy (SEM) Ultra 55 (Zeiss, Germany) on polished samples, using standard metallographic procedure, to mirror-like surface (0.04  $\mu m$ ). The samples are first cut using a microcutting machine along the building direction. They are mounted in a conductive resin using a LaboPress-3 machine (Struers, Denmark) with a 20 kN pressure at 180  $^{\circ}$ C for 6 min followed by water cooling for 3 min. Then, the samples are ground with silicon carbide papers (#320, #1200), polished with a diamond suspension spray for 10 min (3  $\mu m$ ), 10 min (1  $\mu m$ ) and finally using an oxide polishing suspension (OPS) containing 0.04  $\mu m$  silica particles for at least 45 min.

In order to perform the healing heat treatment (HHT), the samples were first sealed inside a Quartz tube filled with argon inert atmosphere. Then, they were heat treated for 30 min at three different temperatures (500, 540 or 580 °C) in a furnace (Nabertherm, Germany) and then cooled down at 10 °C/min until room temperature to avoid hot cracking during solidification. Some heat treatments were also performed in a differential scanning calorimetry (DSC) STA 449 F3 Jupiter (Netzsch, Germany) equipment to investigate the amount of liquid phase during the healing. An empty graphite crucible was used as reference and the sample was introduced in another graphite crucible. Both crucibles were closed with a graphite lid. The heating procedure was set to a heating rate of 10 °C/min up to 660 °C and then cooled down to room

temperature at 10 °C/min.

The static mechanical properties were studied according to ASTM-E8M - 15 a standard using a 50 kN tensile machine (Zwick/Roell, Switzerland). The specimens were machined by electrical discharge machining to get a thickness of 1.5 mm, a reduced section length of 26 mm and a width of 6 mm. They were then prepared for mechanical testing by polishing the surface up to #1200 grit sandpaper by hand. The extension rate of the test was 1 mm/min and samples were loaded until fracture. Three samples were tested for each condition and their results were averaged.

X-ray nano-holo-tomography (nano-CT) was performed on beamline ID16B at the European Synchrotron Radiation Facility (ESRF, Grenoble, France) [34]. Tensile specimens were pulled until fracture and nano-CT samples were extracted close to the fracture surface in order to maximise the damage content in the sample before healing. The samples were mounted on an alumina tube using cement glue (to resist high temperatures) and this alumina tube was fixed on a brass holder in order to be fit on the beamline and in the furnace. The beamline was equipped with a dedicated furnace. It was therefore possible to apply a heat treatment in between scans without moving the sample. The damaged samples were scanned before and after HHT (30 min at 500, 540 or 580 °C followed by a cooling rate of 10 °C/min) in order to follow the damage healing evolution.

One scan acquires 3004 projections over the 360° revolution of the sample, with an exposure time of 45 ms per step. A conic pink beam ( $\Delta E/E=10\text{--}2)$  with an energy of 17.5 keV was used. Two scans were performed for the HHT at 540 °C: a full sample scan at a voxel size of 200 nm and a region of interest (ROI) scan at a voxel size of 35 nm. For the other temperature conditions, only the high-resolution scan on the ROI was performed with the voxel size of 35 nm. The ROI was a cylinder of 75  $\mu m$  diameter and 90  $\mu m$  height.

After the nano-CT experiment, plasma focused ion beam scanning electron microscopy (PFIB-SEM) and electron dispersive x-ray spectroscopy (EDX) were performed to investigate the healing mechanism on the exact same ROI analysed previously by the nano-CT of the samples healed at 540  $^{\circ}$ C. First, the sample was glued to a sample holder (Thermo Fisher Scientific, USA), containing fiducial markers for multimodal data registration, and a whole volume of a sample was scanned with voxel size of 2 µm using a µCT lab-based Nanotom system (Waygate Technologies, Germany). µCT based data were co-registered with the holder surface SEM images and nano-CT based data in order to define the specific ROI coordinates within the µCT images and to be traced further with PFIB-SEM. After precise determination of the ROI, a serial sectioning tomography using the automated Xe PFIB Helios Hydra DualBeam (Thermo Fisher Scientific, USA) combined with the acquisition of SEM back-scattered electron images (voxel size 60 nm) was launched. The correlative analysis was then performed using the software Avizo 3D 2021.1.

In order to identify the healing mechanism of the eutectic-based healing strategy, a heating in-situ SEM experiment was performed on polished cylindrical samples of 5 mm diameter and 1–2 mm thickness. These samples were heated in a Clara SEM (Tescan, Czech Republic) fitted with a FurnaSEM heating stage (NewTec Scientific, France). The sample was mounted alongside a roughened piece of Zr to act as a getter for residual oxygen in the chamber. High resolution images were taken prior to experiment in a high vacuum mode. The sample was then heated up to 200  $^{\circ}\text{C}$  at 2  $^{\circ}\text{C/s}$  for 10 min to allow the carbon cement holding the sample to degas. Oxygen-free nitrogen was introduced into the SEM to reach a pressure of 200 Pa to prevent Mg sublimation. Note that the presence of nitrogen decreases the quality of the obtained images due to scattering of the electron beam. Finally, the sample was heated up to 500  $^{\circ}$ C at 2  $^{\circ}$ C/s and held for one hour with secondary electron images taken every 20 s. 500 °C was selected to avoid the Mg sublimation at the selected pressure. However, the healing effect should be observed at 500 °C (Fig. 4). The sample was then cooled down at 2 °C/s to room temperature. The SEM was set back in high vacuum in order to be able to

obtain subsequent high-resolution images.

### 4. Results and discussion

### 4.1. Microstructure of as-built alloy

SEM provides a comprehensive picture of the HA network within the produced alloy (Fig. 3a and b). The structural matrix is composed of cells  $0.7 \pm 0.2~\mu m$  width (in light grey) surrounded by the eutectic HA network with  $60 \pm 25~nm$  of average wall thickness network which has a melting temperature of 450 °C according to the well-established binary phase diagram [32]. This bi-phasic structure has been characterised in 3D by PFIB-SEM. As the main challenge of healable metallic alloys is the low mobility of their atoms [17], this highly interconnected network of HA surrounding the  $\alpha$ -Al cells (Fig. 3b and Supplementary Movie S1) is key to ensure the flow of HA towards damage and maximize the healing efficiency of the material, similarly to a vascular network. This confirms the interest of LPBF to manufacture liquid healable alloys.

# 4.2. Damage mechanism and related healing potential

In order to investigate the healability of AlMg8, it is important to characterise and understand the damage mechanism of this alloy. Fig. 3c-d highlight this damage mechanism under tensile forces. Damage first nucleates by fracture of the brittle eutectic network and then propagates along it. Damage sites are therefore, as required, highly accessible by the HA flow during HHT as it is initiated at the boundaries of the HA vascular network itself. Moreover, damage preferentially propagates along the network and not within the tougher  $\alpha$ -Al cells. The width of the damage sites to be healed is thus of the same order of magnitude as the network thickness ranging between 35 and 85 nm. This is not the case of LPBF defects such as porosities which are distributed inside the entire material, meaning within cells or within the HA network. However, their size is usually larger than the cell size, meaning that they should always be in contact with a HA source and might thus also expect to be reached and healed by the HA.

The worst-case scenario would be a small void located in the middle of a cell but as already mentioned this is unlikely to occur. In that case, a different microscopic healing mechanism based on diffusion [18,19,35] could be of interest as the  $\alpha$ -Al cells stay in solid state during HHT. Note that this diffusion-based healing mechanism was not experimentally investigated in this paper as the damage sites are located on the HA network itself and could thus be healed by liquid HA flow. However, if required, the use of a diffusion-based healing mechanism could help the closure of voids not accessible by the HA. For this, a supersaturated solid solution composed of fast diffusion rate alloying elements such as Mg, which has already shown some diffusional healing potential [19,35], is required. [36,37] The atoms in supersaturated solution are expected to precipitate during additional heat treatment on the void surfaces. The driving force to trigger this porosity closure is reported to be the decrease in interfacial energy, achieved by a reduction in free surface area per unit volume. [35] Further research will investigate this healing mechanism but, as stated previously, it is not expected to be required for this LPBF AlMg8 alloy.

# 4.3. Selection of the healing temperature and time

An increase of the temperature is required in order to trigger the flow of the molten HA. Therefore, a temperature allowing at least the melting of the HA should be selected. According to the binary phase diagram (Fig. 1d), the eutectic phase starts melting at 450 °C and more liquid phase can be obtained if desired with a temperature higher than 506 °C (melting of the  $\alpha$ -Al phase) but below 610 °C to prevent the alloy from melting completely. 15 wt% of liquid fraction is recommended for liquid phase sintering as it is a good compromise between availability of liquid while maintaining the structural integrity of the part [38]. Differential

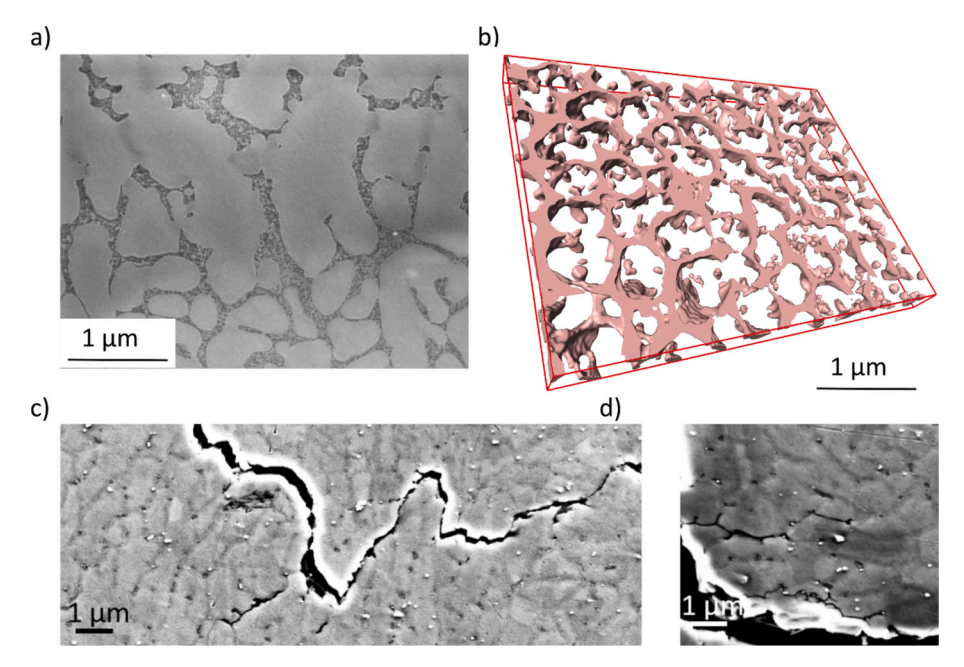


Fig. 3. A) SEM micrograph of the microstructure composed of  $\alpha$ -al cells surrounded by the eutectic phase, b) 3D rendering of the eutectic network of the as-processed AlMg8 alloy obtained by PFIB-SEM, c) and d) SEM images of the mid-section of a fractured tensile sample.

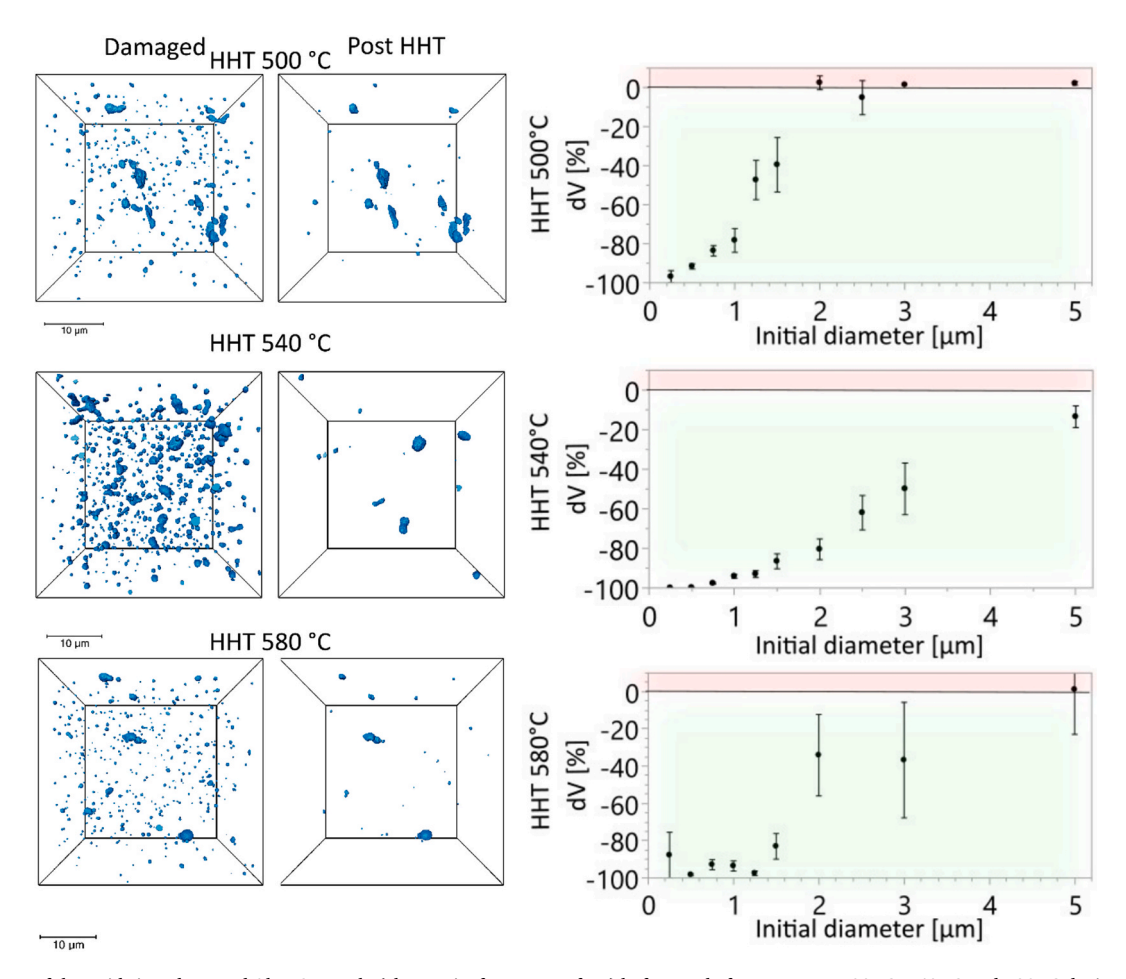


Fig. 4. 3D volume of the voids in a damaged AlMg8 sample (close to its fracture surface) before and after a HHT at 500 °C, 540 °C and 580 °C during 30 min in argon atmosphere obtained by nano-CT at ESRF with a voxel size of 35 nm. Only the voids with a size larger than 3 voxels diameter are represented. The corresponding void evolution as a function of the initial diameter range in the damaged AlMg8 sample is represented with the green and red areas corresponding to voids shrinkage and growth respectively. dV is the percentage of healed volume of a void calculated by  $100 \cdot V_{healed} - V_{damaged}/V_{damaged}$ . The initial diameters were divided into initial diameters ranges and for each range, the average (black point on the graph) and standard deviation of the dV were calculated (error bars on the graph). (For interpretation of the references to colour in this figure legend, the reader is referred to the web version of this article.)

scanning calorimetry (DSC) reveals the liquid fraction, i.e. HA fraction, as a function of temperature (Fig. 1e, see Fig. S7 for the whole DSC curve). Note that the fraction of eutectic phase measured by DSC curve (about 1 %) is much lower than the 20 % of eutectic measured by 2D analysis of SEM images. This is attributed to the diffusion towards the stable microstructure during the heating ramp up to 450 °C at 10 °C/min. Indeed, as observed on the binary phase diagram (Fig. 1d), this large amount of eutectic phase is not expected in this alloy composition and is due to the microsegregation during rapid solidification. Therefore, during the 40 min of heating from room temperature up to 450 °C of the DSC experiment, energy is given to the system to diffuse towards the stable microstructure. There is thus not enough liquid fraction at 450 °C for healing and temperatures in the mushy zone should also be investigated.

To better select the healing heat treatment conditions, nano-CT experiments were conducted on damaged samples at ESRF before and after healing heat treatment (HHT) for 30 min (Fig. 4). These 30 min were chosen based on Fig. 1f which shows the distance travelled by horizontal capillarity flow of liquid pure Al at 660 °C through a horizontal single capillarity tube of uniform circular cross-section of radius r not in contact with the atmosphere, i.e. the atmospheric pressure and the gravity are neglected. The tube is so small that Poiseuille covers practically the whole flow which can therefore be calculated using the simplified Washburn Equation [29] as a function of time for different network thicknesses. Note that these results are calculated using data of pure liquid Al at 660 °C. However, Mg is one of the alloying elements which induces the largest surface tension reduction in liquid Al [39]. This means that better wetting is expected for the HA than for pure liquid Al. As the network thickness varies between 35 and 85 nm (Fig. 3), the HA should be able to flow along more than 15 cm in 30 min of HHT. 30 min were thus selected for the HHT of this proof-of-concept as it is expected to be more than enough to allow transport of the HA towards all damage

Then, to select the healing temperature, the nano-CT experiments were conducted at three different healing heat treatment temperatures: 500 °C, 540 °C and 580 °C (Fig. 4). The 3D volume of the voids before and after these HHT and the manual tracking for more than 1000 voids per sample is represented on Fig. 4 and summarised in Table 1. For all the analysed temperatures, the voids below 1  $\mu m$  were significantly healed.

During the HHT at 500 °C, the HA is only composed of the eutectic phase which amount decreases from 20 % to 1 % during the HHT as the microstructure tends to its stable state. At that temperature, the voids smaller than 250 nm are not 100 % healed (Fig. 4). However, there is a significant reduction of the volume of the voids up to 1  $\mu m$ . Voids larger than 2  $\mu m$  are not significantly healed (Fig. 4). Table 1 shows that there is a significant reduction in the number of the voids while the total void volume reduction is about 15 %.

During the HHT at 540 °C, it is not only the eutectic phase which melts and acts as HA but also part of the  $\alpha$ -Al phase. At this temperature, at least 13 % of liquid is formed according to the DSC experiment (Fig. 1e), which is similar to the 15 % recommended in liquid phase sintering [38]. This larger amount of HA induces a clear decrease of 95 % of the voids number which corresponds to a reduction of 42 % of the total voids volume (Table 1). It can be seen that a significant number of

 $\label{eq:total_problem} \begin{tabular}{ll} \textbf{Table 1} \\ \textbf{Number N, total volume V of voids and total voids reduction volume dV} = 100 \bullet \\ \textbf{V}_{healed} - \textbf{V}_{damaged} / \textbf{V}_{damaged} \begin{tabular}{ll} \textbf{before and after HHT at the different investigated temperatures and the resulting reduction of volume due to the HHT.} \end{tabular}$ 

T <sub>HHT</sub> [°C]	$\begin{array}{c} Damaged \\ N_{voids} \end{array}$	$\begin{array}{c} Healed \\ N_{voids} \end{array}$	Damaged V <sub>voids</sub> [µm <sup>3</sup> ]	Healed V <sub>voids</sub> [µm³]	dV[%]
500	2875	494	1701	1440	-15
540	4323	199	2277	1306	-42
580	3935	379	1035	475	-54

the voids below 2  $\mu m$  are fully or at least partially healed but the effect is less significantly observed on the larger voids (equivalent diameter around 10  $\mu m$ ) (Fig. 4). During the HHT at 540 °C, the larger amount of HA increases void filling ratio improving thus the healing efficiency.

During the HHT at 580  $^{\circ}$ C, at least 40 % of HA is formed according to the DSC experiment (Fig. 1e). This large amount of liquid phase during the healing is too high to maintain the structural integrity of the part as distortions of samples were observed (Fig. 5). This temperature for the HHT was therefore disregarded even if it leads to a significant decrease of 90 % of the voids number which corresponds to a reduction of 54 % of the total voids volume. One could therefore conclude that this increase HA amount leads to a better healing efficiency. However, Fig. 4 shows that no large porosity was by chance present in this damaged sample, and it was already mentioned that small voids are easier to heal. This might therefore also explain the larger reduction in volume compared to the other HHT. It is important to keep the initial voids distribution in mind, as it may vary in the different samples. Indeed, Fig. 4 shows a similar volume reduction for the small voids (below  $2 \mu m$ ) for  $540 \, ^{\circ} C$  and 580 °C. However, there is a significant variability of dV for voids larger than 2 µm at 580 °C. Some even grow, which was not observed at lower temperatures. This might also be due to the too large liquid fraction.

Based on the results of the nano-CT and the 3D tracking of the voids, the HHT at  $540\,^{\circ}$ C, which induces the melting of approximately 15 wt% of HA as recommended in the liquid phase sintering literature [38], is the most efficient. It will thus be selected and further analysed in this proof-of-concept.

# 4.4. Effect of damage size on healing

Two types of voids are expected within damaged tensile specimens produced by LPBF: (i) LPBF defects, i.e initial porosities generated during the LPBF process, which are large (from few  $\mu m$  to hundreds of  $\mu m$  [40]) and usually contain gas [40] and (ii) damage present as voids or microcracks nucleating due to the tensile stresses, which in this case are narrow cracks of approximately 100 nm width appearing at the boundaries of the eutectic network. The largest voids, which were only partially healed, are therefore LPBF defects filled with gas which may hinder the healing due to gas pressure or oxidation. Indeed, to heal these defects, an additional diffusion of this gas through the material in order to escape towards the free surfaces would be required. Another hypothesis would be that there is not enough HA to completely heal such large pores.

As damage size about 100 nm is observed, the healing efficiency of damage is close to 100 % (Fig. 4). Therefore, the healing treatment is effective for voids initiated after an overload. However, the healing of LPBF defects is less effective (Fig. 4) probably because they are usually larger than 2  $\mu m$  and contain gas. The LPBF process must thus be carefully optimised [33,41] or post-treatment applied (such as liquid healing HIP [14,42]) in order to minimise LPBF defects that are too large to be healed without the application of any pressure.



Fig. 5. Distortion of a tensile specimen observed after a heat treatment at 580  $^{\circ}\text{C}.$ 

### 4.5. Effect of healing on the tensile strength

The mechanical properties of an AlMg8 alloy with and without a heat treatment (HT) similar to the HHT (540 °C during 30 min) are shown on Fig. 6. Note that the samples were not damaged before the heat treatment of 30 min at 540 °C. This is why it is called HT and not HHT. This HT induces a slight increase of the yield strength (from  $159\pm22$  MPa to  $164\pm8$  MPa) and does not show any significant effect on the fracture strain (from  $24\pm4$ % to  $25\pm2$ %) of the material. It means that the alloy keeps its mechanical properties or slightly improves them with the HT. This component could thus potentially be further used for the same application after its healing. This increased strength might be due to the stable microstructure obtained after the HHT (Fig. 7b), i.e. 100 % FCC  $\alpha$ -Al with all Mg atoms in solid solution. Indeed, yield strength models usually make the assumption that the individual strength contributions can be added linearly [43] resulting in the following expression:

$$\Delta \sigma_{y} = \Delta \sigma_{DW} + \Delta \sigma_{ss} + \Delta \sigma_{prec} + \Delta \sigma_{GB}$$

where  $\Delta\sigma_{DW}$  is the dislocation walls strengthening,  $\Delta\sigma_{ss}$  is the solute strengthening,  $\Delta\sigma_{prec}$  is the precipitate strengthening and  $\Delta\sigma_{GB}$  is the grain boundary strengthening. During the HT, precipitates are dissolved, reducing thus the precipitate strengthening contribution. Grains are expected to either stay at the same size or grow due to the HT. This means that the  $\Delta\sigma_{GB}$  could also have slightly decreased. Moreover, a decrease of the dislocation density due to recovery can be expected decreasing the dislocation contribution. The last contribution is due to solute strengthening which is usually defined as  $\Delta\sigma_{SS} = HC^{\alpha}$  where  $\alpha$  and H are constant parameters while C is the weight concentration of Mg in solid solution [43,44]. Mukai *et al.* used 13.8 MPa/wt% and 1 for  $\alpha$  [44]. This means that  $\Delta\sigma_{SS}$  is approximately 115 MPa. This contribution is thus expected to be the main contribution to strengthening.

# 4.6. Investigating the healing mechanism

The volume of interest previously analysed by nano-CT was further analysed by PFIB-SEM-EDX in order to investigate the difference between the healed and partially healed areas (Fig. 7c-f). The healed areas (Fig. 7c) are completely welded and have the same chemical composition as the matrix. This means that these defects are completely healed during the HHT. The surface of partially healed voids which are typically LPBF defects or too large damage sites was enriched in Mg compared to the matrix composition. This means that Mg, and thus liquid HA, migrated towards the cavity, but complete healing and then homogenisation could not be achieved. This could be due to insufficient amount of HA. Another explanation might be due to the presence of gas such as

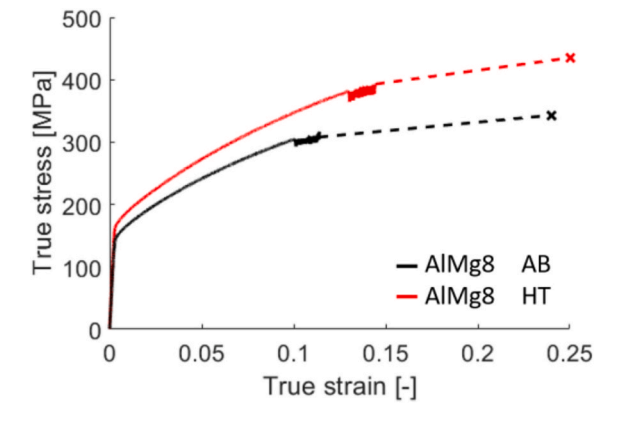


**Fig. 6.** Representative true tensile curve of an as-built (AB) sample (in black) and a heat-treated sample at 540  $^{\circ}$ C for 30 min (in red). (For interpretation of the references to colour in this figure legend, the reader is referred to the web version of this article.)

hydrogen inside the voids if the void is a LPBF defect.

Fig. 7g-i shows the healing of two voids (of approximately 2  $\mu m$  and 1.2  $\mu m$  diameter) at 500 °C in argon atmosphere during in-situ SEM heating. The complete healing of these voids can be observed in the Supplementary Movie S2. After 10 min, the voids are completely healed. This is indeed the predicted healing time by HA flow (Fig. 1f).

One of the reasonable questions about healing of voids is "where is this new volume which filled the void coming from?". There are no clear and obvious answers at this stage, however, we suggest here a few hypotheses:

- 1) The first hypothesis mentioned in Ref. [45] states that the system is closed, meaning that the volume which filled the void should come from another location in the part. This means that we have thus only transfer of the void from one to another location where it is less harmful. In order to verify this first hypothesis, the total volume of the voids was measured before and after healing heat treatment. Table 1 shows that the number of voids within the same volume of interest is decreased by 96 % during the HHT at 540 °C (corresponding to a reduction of 43 % of the void volume). This means that if the voids volume is still present in the part, the size of these voids is lower than the resolution limit of nano-CT (voxel size of 35 nm) or these voids were transferred outside of the volume of interest.
- 2) The second hypothesis investigated in this work is that no new volume is created but the part shrinks during the healing heat treatment. In order to analyse this hypothesis, the entire volume of a sample was scanned by nano-CT with a voxel size of 200 nm before and after healing. No change in the part dimensions were observed. The total volume of the sample even slightly increased of approximately 0.15 % from  $3.2745 \times 10^7 \ \mu m^3$  to  $3.2797 \times 10^7 \ \mu m^3$ .
- 3) The last hypothesis is that the new volume expansion during the healing is due to phase transformation and/or release of the residual stresses induced during LPBF. Indeed, the microstructure is first composed of approximately 80 vol% of α-Al cells surrounded by 20 vol% of a eutectic network (Fig. 3a). After healing, the microstructure is entirely  $\alpha$ -Al with Mg in solid solution (Fig. 7b). This phase transformation and reorganisation of the atoms might be the reason of this volume increase. Indeed, we can perform a quick back of the envelope calculation of the average lattice parameter before and after healing. Based on SEM images analysis (from the PFIB-SEM experiment used to make Fig. 3b), the as-built sample is composed of maximum 10 % of the Samson phase β-Al<sub>3</sub>Mg<sub>2</sub>. This phase has a complex lattice structure of parameter 28.2 Å but containing 1168 atoms [46]. There is also approximately 90 % of  $\alpha$ -Al phase which has a lattice parameter of 4.05 Å but contains only 4 atoms [47]. In order to compare both lattices, the cubic volume occupied by 4 atoms in the Samson phase is calculated and is 4.25 Å. It means that in the as-built sample, the mean cubic volume occupied by 4 atoms is 0.9 \* 4.05 + 0.1 \* 4.25 = 4.06 Å. The healed sample is composed of 100 % of α-Al phase distorted due to the presence of all the Mg in solid solution. This results in a lattice parameter of 4.09 Å, also occupied by 4 atoms [47]. In conclusion, this would mean that there is thus an increase of approximately 0.7 % of the mean cubic volume occupied by 4 atoms with the healing heat treatment due to the phase transformation. Comparatively, as discussed above in the second hypothesis, the HHT was shown to bring a total volume increase of approximately 0.15 %. Note that these are estimated calculations based on strong assumptions such as the absence of Mg in solid solution in the as-built  $\alpha$ -Al cells and the absence of residual stresses in the as-built material which could distort the lattice.

# 5. Conclusions

In conclusion, the liquid phase assisted healing efficiency of the binary LPBF Al-Mg alloy is close to 100 % and could increase the lifetime of parts subjected to an overload. Damage up to 2  $\mu$ m was efficiently

J. Gheysen et al. Materials & Design 258 (2025) 114573

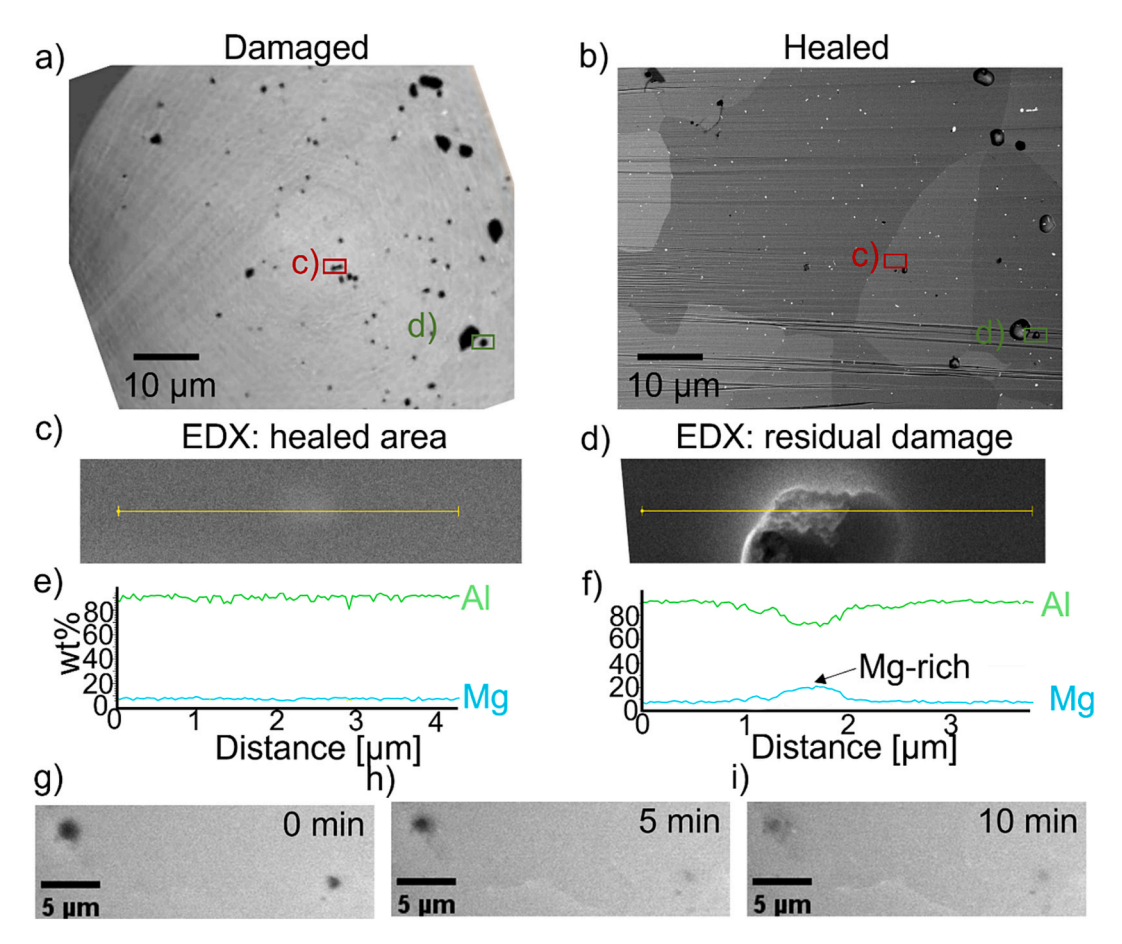


Fig. 7. Cross section extracted a) from nano-CT volumes and b) by PFIB-SEM of a damaged sample a) before and b) after HHT at 540 °C. The healed area in c) and the residual damage area in d) were further analyzed by EDS in e) and f) respectively. A two voids area was observed by SEM during in-situ healing at 500 °C after g) 0 min, h) 5 min and i) 10 min.

healed, while larger LPBF defects were only partially healed. Correlative imaging highlighted the complete healing and welding of these voids within less than 10 min. It also highlighted the contribution of Mg in the healing mechanism. This concept may potentially also be applicable to a broad class of hypo- and hyper-eutectic LPBF alloys such as for example the high strength Al 7075 alloy or 2xxx series Al alloys which shows a eutectic temperature of approximately 480 °C and 548 °C respectively, as well as a similar vascular network. This technique might also be used with other manufacturing technologies. However, if the microstructure is coarser than the one obtained with LPBF, it might be necessary to significantly increase the HHT time in order to let enough time for transport of the healing agent towards the damage sites. LPBF is thus perfectly suited for the development of self-healing materials as it produces a eutectic structure similar to the vascular network found within living systems. Finally, this new healable Al alloy is rather inexpensive and composed of readily available materials, thus convenient for a wide range of applications, including aeronautic and aerospace industries. It will just, in the future, require adding a precipitation hardening mechanism for its mechanical strength to reach the requirements of the industries.

# CRediT authorship contribution statement

Julie Gheysen: Writing – original draft, Visualization, Validation, Methodology, Investigation, Formal analysis, Data curation, Conceptualization. Grzegorz Pyka: Writing – review & editing, Supervision, Methodology, Conceptualization. Bartłomiej Winiarski: Writing – review & editing, Supervision, Methodology, Conceptualization. Julie Villanova: Writing – review & editing, Methodology,

Conceptualization. Florent Hannard: Writing – review & editing, Methodology, Investigation. Sophie De Raedemacker: Writing – review & editing, Investigation. Jack Donoghue: Methodology, Investigation, Conceptualization. Albert Smith: Methodology, Investigation, Conceptualization. Aude Simar: Writing – review & editing, Supervision, Resources, Funding acquisition, Formal analysis.

# Funding

J.G. is supported by the Fonds de la recherche scientifique – FNRS (FRIA grant  $\rm n^{\circ}35482530)$ , Belgium. Consumables and A.S are funded by the European Research Council (ERC) (grant agreement  $\rm n^{\circ}716678)$ . We acknowledge the European Synchrotron Radiation Facility for provision of synchrotron radiation facilities (proposal MA4874). Avizo software acquisition was supported by the Fonds de la Recherche Scientifique – FNRS – EQP under grant UN06920F. The publication was supported by the Fondation Universitaire de Belgique. This publication is part of the project HAMAAC of the research program 2022-1, which has been supported by M-ERA.NET under the grant 2210137.

### Declaration of competing interest

The authors declare that they have no known competing financial interests or personal relationships that could have appeared to influence the work reported in this paper.

# Acknowledgments

We acknowledge the European Synchrotron Radiation Facility

(ESRF) for provision of synchrotron radiation facilities (experiment MA4874 and inhouse beamtime) and we would like to thank Dr M Arseenko for assistance in using beamline ID16B. We acknowledge Prof. Philip Withers for discussions and the access to the heating in-situ SEM system. We acknowledge Ali Chirazi for the collaboration with ThermoFisher. The LACAMI platform of iMMC/UCLouvain is acknowledged for technical support. Dr Nicolas Nothomb is acknowledged for support the material manufacturing and characterisation related to supplementary Fig. S3.

# Appendix A. Supplementary data

Supplementary data to this article can be found online at https://doi.org/10.1016/j.matdes.2025.114573.

### Data availability

Data will be made available on request.

### References

- [1] R. Cunningham, S.P. Narra, C. Montgomery, J. Beuth, A.D. Rollett, Synchrotron-based X-ray microtomography characterization of the effect of processing variables on porosity formation in laser power-bed additive manufacturing of Ti-6Al-4V, JOM 69 (2017) 479–484, https://doi.org/10.1007/s11837-016-2234-1.
- [2] N. van Dijk, S. van der Zwaag, Self-healing phenomena in metals, Adv. Mater. Interfaces 5 (2018), https://doi.org/10.1002/admi.201800226.
- [3] P. Li, D.H. Warner, J.W. Pegues, M.D. Roach, N. Shamsaei, N. Phan, Investigation of the mechanisms by which hot isostatic pressing improves the fatigue performance of powder bed fused Ti-6Al-4V, Int. J. Fatigue 120 (2019) 342–352, https://doi.org/10.1016/j.iifatigue.2018.10.015.
- [4] A. Röttger, K. Geenen, M. Windmann, F. Binner, W. Theisen, Comparison of microstructure and mechanical properties of 316L austenitic steel processed by selective laser melting with hot-isostatic pressed and cast material, Mater. Sci. Eng. A 678 (2016) 365–376, https://doi.org/10.1016/j.msea.2016.10.012.
- [5] A. Kreitcberg, V. Brailovski, S. Turenne, Effect of heat treatment and hot isostatic pressing on the microstructure and mechanical properties of Inconel 625 alloy processed by laser powder bed fusion, Mater. Sci. Eng. A 689 (2017) 1–10, https:// doi.org/10.1016/j.msea.2017.02.038.
- [6] S. Leuders, M. Thöne, A. Riemer, T. Niendorf, T. Tröster, H.A. Richard, H.J. Maier, On the mechanical behaviour of titanium alloy TiAl6V4 manufactured by selective laser melting: Fatigue resistance and crack growth performance, Int. J. Fatigue 48 (2013) 300–307, https://doi.org/10.1016/j.ijfatigue.2012.11.011.
- [7] M.-W. Wu, J.-K. Chen, B.-H. Lin, P.-H. Chiang, Improved fatigue endurance ratio of additive manufactured Ti-6Al-4V lattice by hot isostatic pressing, Mater. Des. 134 (2017) 163–170, https://doi.org/10.1016/j.matdes.2017.08.048.
- [8] M.-W. Wu, P.-H. Lai, The positive effect of hot isostatic pressing on improving the anisotropies of bending and impact properties in selective laser melted Ti-6Al-4V alloy, Mater. Sci. Eng. A 658 (2016) 429–438, https://doi.org/10.1016/j. msea.2016.02.023.
- [9] T. Mishurova, K. Artzt, B. Rehmer, J. Haubrich, L. Ávila, F. Schoenstein, I. Serrano-Munoz, G. Requena, G. Bruno, Separation of the impact of residual stress and microstructure on the fatigue performance of LPBF Ti-6Al-4V at elevated temperature, Int. J. Fatigue 148 (2021) 106239, https://doi.org/10.1016/j.ijfatigue.2021.106239.
- [10] N.O. Larrosa, W. Wang, N. Read, M.H. Loretto, C. Evans, J. Carr, U. Tradowsky, M. M. Attallah, P.J. Withers, Linking microstructure and processing defects to mechanical properties of selectively laser melted AlSi10Mg alloy, Theor. Appl. Fract. Mech. 98 (2018) 123–133, https://doi.org/10.1016/j.tafmec.2018.09.011.
- [11] C.B. Finfrock, A. Exil, J.D. Carroll, L. Deibler, Effect of hot isostatic pressing and powder feedstock on porosity, microstructure, and mechanical properties of selective laser melted AlSi10Mg, Metallogr. Microstruct. Anal. 7 (2018) 443–456, https://doi.org/10.1007/s13632-018-0456-z.
- [12] J.G. Santos Macías, L. Zhao, D. Tingaud, B. Bacroix, G. Pyka, C. van der Rest, L. Ryelandt, A. Simar, Hot isostatic pressing of laser powder bed fusion AlSi10Mg: parameter identification and mechanical properties, J. Mater. Sci. 57 (2022) 9726–9740, https://doi.org/10.1007/s10853-022-07027-9.
- [13] C. Nyahumwa, Effectiveness of hot isostatic pressing on healing oxide film defects in cast aluminium alloys, Tanzan, J. Eng. Technol. 29 (2006) 43–58, https://doi. org/10.52339/tjet.v29i1.374.
- [14] J. Gheysen, D. Tingaud, J. Villanova, A. Hocini, A. Simar, Exceptional fatigue life and ductility of new liquid healing hot isostatic pressing especially tailored for additive manufactured aluminum alloys, Scr. Mater. 233 (2023) 115512, https:// doi.org/10.1016/j.scriptamat.2023.115512.
- [15] A. Schmets, G. Zaken, S. Zwaag, Self Healing Materials: An Alternative Approach to 20 Centuries of Materials Science, (2007).
- [16] S.R. White, N.R. Sottos, P.H. Geubelle, J.S. Moore, M.R. Kessler, S.R. Sriram, E. N. Brown, S. Viswanathan, Autonomic healing of polymer composites, Nature 409 (2001) 794–797, https://doi.org/10.1038/35057232.

- [17] M. Arseenko, J. Gheysen, F. Hannard, N. Nothomb, A. Simar, Self-healing in metal-based systems, Self-Heal Constr. Mater. Fundam. Monit. Large Scale Appl. (2022) 43–78, https://doi.org/10.1007/978-3-030-86880-2\_3.
- [18] J. Gheysen, A. Kashiwar, H. Idrissi, J. Villanova, A. Simar, Suppressing hydrogen blistering in a magnesium-rich healable laser powder bed fusion aluminum alloy analyzed by in-situ high resolution techniques, Mater. Des. 231 (2023) 112024, https://doi.org/10.1016/j.matdes.2023.112024.
- [19] M. Song, K. Du, S.P. Wen, Z.R. Nie, H.Q. Ye, In situ electron microscopy investigation of void healing in an Al–Mg–Er alloy at a low temperature, Acta Mater. 69 (2014) 236–245, https://doi.org/10.1016/j.actamat.2014.02.004.
- [20] J. Martínez Lucci, R.S. Amano, P.K. Rohatgi, Heat transfer and fluid flow analysis of self-healing in metallic materials, Heat Mass Transf. 53 (2016) 825–848, https://doi.org/10.1007/s00231-016-1837-y.
- [21] J. Martinez Lucci, R.S. Amano, P. Rohatgi, B. Schultz, Experiment and Computational Analysis of Self-Healing in an Aluminum Alloy, ASME 2008 Int. Mech. Eng. Congr. Expo. Volume 10: Heat Transfer, Fluid Flows, and Thermal Systems, Parts A, B, and C (2008) 1759–1768. https://doi.org/10.1115/ imece2008-68304.
- [22] P. Leser, Mitigation of Crack Damage in Metallic Materials, (2014). https://books.google.be/books?id=x6uvuwEACAAJ.
- [23] V. Kilicli, X. Yan, N. Salowitz, P.K. Rohatgi, Recent advancements in self-healing metallic materials and self-healing metal matrix composites, JOM 70 (2018) 846–854, https://doi.org/10.1007/s11837-018-2835-y.
- [24] M. Nosonovsky, P.K. Rohatgi, Development of metallic and metal matrix composite self-healing materials, Biomim. Mater. Sci. (2011) 87–122, https://doi.org/ 10.1007/978-1-4614-0926-7 5.
- [25] J. Kim, H.J. Kim, S.H. Hong, H.J. Park, Y.S. Kim, Y.J. Hwang, Y.B. Jeong, J.-Y. Park, J.M. Park, B. Sarac, W.-M. Wang, J. Eckert, K.B. Kim, Thermally-triggered dual in-situ self-healing metallic materials, Sci. Rep. 8 (2018) 2120, https://doi.org/10.1038/s41598-018-19936-4.
- [26] G. Siroky, E. Kraker, J. Rosc, D. Kieslinger, R. Brunner, S. Van Der Zwaag, E. Kozeschnik, W. Ecker, Analysis of Sn-Bi solders: X-ray micro computed tomography imaging and microstructure characterization in relation to properties and liquid phase healing potential, Materials 14 (2020) 153, https://doi.org/ 10.3390/ma14010153.
- [27] R. Amano, P. Rohatgi, J. Lucci, B. Schultz, A. Ruzek, Design and Demonstration of Self-Healing Behavior in a Lead-Free Solder Alloy, (2009). https://doi.org/ 10.2514/6.2009-4514.
- [28] M. Assael, K. Kakosimos, R. Banish, J. Brillo, I. Egry, R. Brooks, P. Quested, K. Mills, A. Nagashima, Y. Sato, W. Wakeham, Reference data for the density and viscosity of liquid aluminum and liquid iron, J. Phys. Chem. Ref. Data 35 (2006) 285–300, https://doi.org/10.1063/1.2149380.
- [29] E.W. Washburn, The dynamics of capillary flow, Phys. Rev. 17 (1921) 273–283, https://doi.org/10.1103/PhysRev.17.273.
- [30] S. Kou, Solidification and liquation cracking issues in welding, JOM 55 (2003) 37–42, https://doi.org/10.1007/s11837-003-0137-4.
- [31] J.G. Santos Macías, T. Douillard, L. Zhao, E. Maire, P.G.A. Simar, Influence on microstructure, strength and ductility of build platform temperature during laser powder bed fusion of AlSi10Mg, Submitt. Acta Mater. (2020).
- [32] M. Hansen, K. Anderko., Constitution of binary alloys (Second edition), 18 (1958).
- [33] J. Gheysen, M. Marteleur, C. van der Rest, A. Simar, Efficient optimization methodology for laser powder bed fusion parameters to manufacture dense and mechanically sound parts validated on AlSi12 alloy, Mater. Des. 199 (2021) 109433, https://doi.org/10.1016/j.matdes.2020.109433.
- [34] J. Gheysen, M. Arseenko, F. Hannard, E. Maire, G. PYKA, A. SIMAR, J. VILLANOVA, Investigation by 3D nano-holotomography of the self-healability of an Aluminium alloy produced by additive manufacturing, (2021). https://doi.org/10.15151/ESRF-ES-449124708.
- [35] M. Arseenko, F. Hannard, L. Ding, L. Zhao, E. Maire, J. Villanova, H. Idrissi, A. Simar, A new healing strategy for metals: programmed damage and repair, Acta Mater. 238 (2022) 118241, https://doi.org/10.1016/j.actamat.2022.118241.
- [36] S. Hautakangas, H. Schut, N.H. van Dijk, P.E.J. Rivera Díaz del Castillo, S. van der Zwaag, Self-healing of deformation damage in underaged Al-Cu-Mg alloys, Scr. Mater. 58 (2008) 719–722, https://doi.org/10.1016/j.scriptamat.2007.11.039.
- [37] R.N. Lumley, G.B. Schaffer, Precipitation induced densification in a sintered Al–Zn–Mg–Cu alloy, Scr. Mater. 55 (2006) 207–210, https://doi.org/10.1016/j. scriptamat.2006.04.021.
- [38] R.M. German, Chapter nine sintering with a liquid phase, Sinter Empir. Obs. Sci. Princ. (2014) 247–303, https://doi.org/10.1016/B978-0-12-401682-8.00009-4.
- [39] I.F. Bainbridge, J.A. Taylor, The surface tension of pure aluminum and aluminum alloys, Metall. Mater. Trans. A 44 (2013) 3901–3909, https://doi.org/10.1007/ s11661-013-1696-9.
- [40] G.K.L. Ng, A.E.W. Jarfors, G. Bi, H.Y. Zheng, Porosity formation and gas bubble retention in laser metal deposition, Appl. Phys. A 97 (2009) 641, https://doi.org/ 10.1007/s00339-009-5266-3.
- [41] K. Kempen, L. Thijs, J. Van Humbeeck, J.P. Kruth, Processing AlSi10Mg by selective laser melting: parameter optimisation and material characterisation, Mater. Sci. Technol. 31 (2015) 917–923, https://doi.org/10.1179/ 1743284714Y.0000000702.
- [42] J. Gheysen, Design, development and characterisation of new healable laser powder bed fusion aluminium alloys, Thesis, 2022.
- [43] E.L. Huskins, B. Cao, K.T. Ramesh, Strengthening mechanisms in an Al-Mg alloy, Mater. Sci. Eng. A 527 (2010) 1292–1298, https://doi.org/10.1016/j. msea 2000 11 056
- [44] T. Mukai, K. Higashi, S. Tanimura, Influence of the magnesium concentration on the relationship between fracture mechanism and strain rate in high purity Al–Mg

- alloys, Mater. Sci. Eng. A 176 (1994) 181-189, https://doi.org/10.1016/0921-5093(94)90974-1.
- [45] S. van der Zwaag, E. Brinkman, I.O.S. Press, Self healing materials: pioneering
- research in the Netherlands, (2015). http://site.ebrary.com/id/11138172.

  [46] A. Zielinska-Lipiec, B. Dubiel, A. Czyrska-Filemonowicz, Microstructure of the complex metallic β-Al3Mg2 phase, Inzynieria Mater. 175 (2010) 562–564.
- [47] B.B. Straumal, B. Baretzky, A.A. Mazilkin, F. Phillipp, O.A. Kogtenkova, M. N. Volkov, R.Z. Valiev, Formation of nanograined structure and decomposition of supersaturated solid solution during high pressure torsion of Al–Zn and Al–Mg alloys, Acta Mater. 52 (2004) 4469–4478, https://doi.org/10.1016/j. actamat.2004.06.006.